Latitudinal variations in Saturn's ionosphere: Cassini measurements and model comparisons

Luke Moore,[1] Ingo Mueller-Wodarg,[2] Marina Galand,[2] Arvydas Kliore,[3] and Michael Mendillo[1]

[1]   We present a study of latitudinal variations in Saturn's ionosphere using Cassini Radio Science Subsystem (RSS) measurements and Saturn-Thermosphere-Ionosphere-Model (STIM) simulations. On the basis of Cassini RSS observations, the peak electron density (N_{MAX}) and the total electron content (TEC) both exhibit a clear increase with latitude, with a minimum at Saturn's equator. When compared with these RSS trends, current model simulations overestimate N_{MAX} and TEC at low latitudes and underestimate those parameters at middle and high latitudes. STIM is able to reproduce the RSS values for N_{MAX} and TEC at low latitude when an additional low-latitude loss process, such as a water influx, is introduced near Saturn's equator. The lack of auroral precipitation processes in the model likely explains some model/data discrepancies at high latitude; however, most of the high-latitude RSS data are from latitudes outside of Saturn's typical main auroral oval. Using Cassini RSS electron density altitude profiles combined with ion density fractions and neutral background parameters calculated in STIM, we also present estimates of the latitudinal variations of Saturn's Pedersen conductance, Σ_P. We find Σ_P to be driven by ion densities in Saturn's lower ionosphere and to exhibit a latitudinal trend with a peak at mid-latitude. Model calculations are able to reproduce low-latitude conductances when an additional loss process is introduced, as before, but consistently underestimate most of the mid- and high-latitude conductances derived from Cassini observations, perhaps indicating a missing ionization source within the model.

1. Introduction

[2]   The technique of radio occultation, wherein Saturn's atmosphere occults the transmission of a radio signal from a spacecraft to Earth [e.g., *Kliore et al.*, 2004], provides the only available remote diagnostic of electron density altitude profiles, $N_e(h)$, a basic ionospheric property. There have been 37 radio occultations of Saturn's ionosphere published to date: two each by the Pioneer 11, Voyager 1, and Voyager 2 spacecraft during their flybys of the Saturn system on 1 September 1979, 12 November 1980, and 26 August 1981, respectively [*Atreya et al.*, 1984], and 31 by the Cassini spacecraft in the 6 years since its insertion into Saturn orbit on 1 July 2004 [*Nagy et al.*, 2006; *Kliore et al.*, 2009]. Analysis of this relatively sparse data set is both complicated and enriched by the fact that radio occultations have sampled a full range of latitudes, seasons, and incident solar irra-

diances at Saturn. Furthermore, there is a high degree of variability among the derived $N_e(h)$ profiles, even for those with similar background conditions.

[3]   Early studies of the Saturn ionosphere were primarily focused on understanding the basic processes responsible for controlling the peak ionospheric density, N_{MAX}, as prior theoretical predictions of N_{MAX} at $\sim 10^5$ e$^-$ cm^{-3} [*McElroy*, 1973; *Atreya and Donahue*, 1975; *Capone et al.*, 1977; *Waite et al.*, 1979] were found to be about an order of magnitude larger than those observed by the Pioneer 11 [*Kliore et al.*, 1980a, 1980b], Voyager 1 [*Tyler et al.*, 1981], and Voyager 2 spacecraft [*Tyler et al.*, 1982; *Lindal et al.*, 1985]. This overestimate was initially thought to be caused by the long chemical lifetime of the predicted major ion, H$^+$, and therefore, beginning in the 1980s, subsequent models of the Saturn ionosphere included mechanisms for converting the long-lived protons into shorter-lived molecular ions, thereby reducing the modeled electron densities to better match observed values. The first such mechanism considered was charge exchange between H$^+$ and vibrationally excited H$_2$ (in the fourth or higher vibrational state), as originally suggested by *McElroy* [1973]. The second candidate mechanism studied was charge exchange between H$^+$ and water molecules originating from Saturn's rings and/or icy moons [*Connerney and*

---

[1]Center for Space Physics, Boston University, Boston, Massachusetts, USA.
[2]Department of Physics, Imperial College London, London, UK.
[3]Radio Science Systems, Jet Propulsion Laboratory, Pasadena, California, USA.

Waite, 1984]. Both mechanisms have proven difficult to constrain independently. While there have been spectroscopic measurements of water in Saturn's atmosphere [*Feuchtgruber et al.*, 1997; *Prangé et al.*, 2006] from which it is possible to estimate a global [e.g., *Moses et al.*, 2000] or local water influx [*Prangé et al.*, 2006], it is not clear how variable such an influx would be. There are no available measurements to constrain Saturn's H_2 vibrational levels, yet they must be populated to some degree, as the main source mechanisms creating vibrationally excited H_2 are collisions of H_2 with electrons [*Hallett et al.*, 2005] and H_3^+ electron recombination (two processes thought to continuously occur in Saturn's ionosphere). Therefore, while modeling studies have been performed that evaluate H^+ loss due to charge exchange with both $H_2(\nu \geq 4)$ and H_2O [e.g., *Majeed and McConnell*, 1991, 1996; *Moses and Bass*, 2000; *Moore et al.*, 2004], and while model calculations have been able to reproduce average trends present in Cassini radio occultations [*Moore et al.*, 2006], there is no general consensus on the relative importance of each of these loss processes in Saturn's ionosphere. A more comprehensive review of our current understanding of Saturn's ionosphere may be found in the work of *Nagy et al.* [2009].

[4] The current picture of Saturn's ionosphere given by radio occultation measurements and the associated modeling is summarized in the following: (1) There is a large degree of variability in the available electron density profiles. This variability can be partially explained by differences in the solar zenith angles of the measurements, via the different latitudes and seasons, but substantial inherent variability remains unexplained. (2) Despite the variability in the measurements, averages of the Cassini observations show two consistent trends: a dawn/dusk asymmetry, where dawn $N_e(h)$ profiles typically have a lower peak electron density and a higher peak altitude, h_{MAX}, than dusk $N_e(h)$ profiles [*Nagy et al.*, 2006] and an increase in N_{MAX} with latitude with a minimum at Saturn's equator [*Kliore et al.*, 2009]. The former trend may be accounted for by the local time patterns of atomic and molecular ions: Molecular ions recombine quickly during the Saturn night, leaving primarily the atomic ion plasma at dawn [*Moore et al.*, 2006]. *Kliore et al.* [2009] suggest some combination of particle precipitation and water influx as a possible explanation of the trend of an increasing N_{MAX} with latitude; however, no further quantitative investigation of this scheme has yet been performed. (3) Cassini radio occultation measurements span $-74.1°$ to $+75.4°$ in latitude, $-24.5°$ to $-6°$ in solar declination, and 116 to 66 in solar F10.7 indices [*Nagy et al.*, 2006; *Kliore et al.*, 2009]. Thus, there is a considerable range of background conditions for each of the 37 observations, making each unique.

[5] This study seeks to bridge these three topics using a suite of state-of-the-art models of Saturn's upper atmosphere. Specifically, by making use of the additional $N_e(h)$ profiles and latitudinal coverage now available from Cassini Radio Science Subsystem (RSS), we will move beyond the 1-D model/data comparisons and evaluate latitudinal trends present in the data, then use a series of model calculations to try and understand the origin of those trends. Our approach, including description of the models used, is given in section 2. Electron density trends and accompanying analyses are presented in section 3, while section 4 focuses on latitudinal trends in the ionospheric Pedersen conductance. Finally, section 5 uses the preceding results to lay the basis for a "standard" theoretical groundwork against which future case studies may be compared.

2. Approach

2.1. Model

[6] Rather than attempt tuning model input to reproduce each individual profile separately, we have chosen to study the overall observed trends using a single set of model input conditions for the following reasons: (1) As there is no consensus constraint on ionospheric losses due to charge exchange with H_2O and vibrationally excited H_2, any model reproductions of Cassini $N_e(h)$ profiles would be nonunique. This nonuniqueness could unnecessarily confuse latitudinal model trends. (2) Fixed input conditions in the model allow for a more confident identification of the origin of any resulting trends. (3) It would be computationally prohibitive for the global circulation thermospheric portion of our modeling to reproduce 31 marginally different cases. Moreover, previous studies have shown that Saturn's ionosphere is most sensitive to specified sources of ionization and less sensitive to background atmospheric conditions [e.g., *Moore et al.*, 2004, 2006].

[7] The Saturn Thermosphere-Ionosphere-Model (STIM) is a suite of 1-D, 2-D, and 3-D models of Saturn's upper atmosphere. STIM development began in 2003; it has been updated and improved upon continually since then. The core of STIM is a 3-D global circulation model (GCM) of the Saturn thermosphere, first described by *Mueller-Wodarg et al.* [2006]. Versions of the GCM that include Saturn's ionosphere also exist (although have not yet published, as previous ionospheric studies have focused on parameter space exploration approaches, a poor use computationally of a GCM). Separate 1-D (in altitude) and 2-D (altitude and latitude) ionospheric modules exist that use the thermospheric GCM to define background atmospheric parameters not calculated by the ionospheric modules. These modules include photochemistry, plasma diffusion [*Moore et al.*, 2004], shadowing due to Saturn's rings [*Mendillo et al.*, 2005], and a time-variable water influx [*Moore et al.*, 2006; *Moore and Mendillo*, 2007]. Recently, the ionospheric modules have been coupled with a 1-D electron transport code in order to incorporate the effects of photoelectrons on Saturn's ionosphere [*Galand et al.*, 2009], including plasma temperature calculations [*Moore et al.*, 2008] and parameterizations of the secondary ionization and thermal electron heating rates at Saturn [*Moore et al.*, 2009]. Current model iterations specify Saturn's magnetic field with the Saturn Pioneer Voyager (SPV) model [*Davis and Smith*, 1990]. Calculations using updated magnetic field parameters based on Cassini measurements [e.g., *Russell and Dougherty*, 2010] do not show any discernible differences from those using the SPV model.

[8] Calculations in this study proceed in the following way:

[9] 1. A background GCM run is created for solar minimum conditions at Saturn equinox. The GCM solves globally the coupled nonlinear Navier-Stokes equations of energy, momentum, and continuity for Saturn's major neutral species by explicit time integration. Hydrostatic

equilibrium is assumed in the local vertical direction. This run includes the additions of ion drag, auroral ionization, and Joule heating (based on the rates proposed by *Cowley et al.* [2004]) and updated ion chemistry that includes the hydrocarbon ion species CH_3^+, CH_4^+, and CH_5^+. Through a combination of Joule heating and additional low-latitude empirical heating [see *Mueller-Wodarg et al.*, 2006], this run does a good job of reproducing neutral temperature measurements in the UV [*Smith et al.*, 1983; *Nagy et al.*, 2009] and IR [*Melin et al.*, 2007]. Note that while Joule heating due to auroral ionization provides additional energy to heat the thermosphere to observed levels, only the neutral parameters (e.g., neutral densities, winds, and temperature) are passed to the ionospheric modules discussed later in order to focus on global solar-produced ionospheric trends. Modeling of the auroral ionosphere will be discussed in a separate paper in preparation [*Galand et al.*, 2010].

[10] 2. The 2-D ionospheric module is used, along with the GCM run, which defines the neutral background atmosphere, to create a series of global model ionospheres. This module consists of 45 altitude grid points (covering the range of the GCM) and 91 latitude grid points (2° latitude resolution; −90° to 90°), which are solved simultaneously via explicit time integration. In addition to the processes considered in previous publications [e.g., *Moore et al.*, 2004, 2008], meridional transport along magnetic field lines is now allowed. Meridional transport of ions can arise from meridional ionospheric gradients (which are minimal), neutral winds, and vertical gradient drifts being directed along nonvertical magnetic fields lines. Specifically, the 2-D ionospheric module includes photochemistry, plasma diffusion, ion transport due to neutral winds, ring shadowing effects, ionization due to suprathermal photoelectron, and plasma temperature calculations. The ionospheric module parameterizes the secondary ion production rate due to suprathermal photoelectrons using the method described by *Moore et al.* [2009]. Finally, electron and ion temperatures are calculated based on the parameterizations of the thermal electron heating rate by *Moore et al.* [2008].

[11] As described previously, there is no consensus regarding the relative importance of the $H^+ + H_2O$ and $H^+ + H_2(\nu \geq 4)$ charge exchange reactions. We therefore evaluate a wide range of both processes. The population of H_2 vibrational levels is not calculated self-consistently within the model; rather we start with the distribution described in equation (8) of *Moses and Bass* [2000], and then consider variations of that distribution. Except where stated otherwise, the 2-D ionospheric module uses a solar flux and solar declination (−8.5°) representing the average of the 31 Cassini RSS observations. Solar flux at the top of the atmosphere is specified using the measurements of the Thermosphere Ionosphere Mesosphere Energetics and Dynamics Solar EUV Experiment (TIMED/SEE) extrapolated to Saturn for each of the occultation periods and then averaged together [*Woods et al.*, 2000, 2005; *Woods*, 2008].

2.2. Data Analysis

[12] Although all available Cassini RSS occultation measurements have already been reduced [*Nagy et al.*, 2006; *Kliore et al.*, 2009], there remain regions within the $N_e(h)$ profiles where no electron density is reported. These data gaps are predominantly within the low-altitude ionosphere, where multipath propagation makes it difficult and time-consuming to isolate the one true radio signal from among the many that emerge after being scattered by Saturn's complicated low-altitude ionospheric structures. In some cases, Cassini $N_e(h)$ profiles at high altitude may also drop below the RSS sensitivity, although these are most likely simply indications of Saturn's highly variable ionosphere. While it is beyond the scope of this study to perform, for example, the required additional multipath analysis, profiles with "insufficient data" within these altitude regimes must be identified and eliminated from use in defining the latitude trends to be studied. The criteria for deeming a radio occultation profile "insufficient" for further trend analysis are outlined later.

[13] The calculation of Saturn's ionospheric Pedersen conductance has long been a topic of interest in Saturn's magnetospheric community, as it is a key parameter for describing the currents coupling the ionosphere to the magnetosphere. Prior estimates of Σ_P in the literature, primarily based on Voyager era radio occultations and/or models, cover a wide range of order 0.1 to 100 mho [e.g., *Connerney et al.*, 1983; *Atreya et al.*, 1984; *Cheng and Waite*, 1988]. Theoretical studies, however, use magnetospheric corotation patterns to argue for an effective Pedersen conductance (Σ_P^*) of 1–2 mho [*Bunce et al.*, 2003; *Pontius and Hill*, 2006], later updated to ~4 mho based on comparisons with Cassini and HST data [*Cowley et al.*, 2008].

[14] Cassini's $N_e(h)$ profiles allow an estimate of the variation of Pedersen conductance with latitude for the first time. However, the radio occultations give no indication of ion species or neutral densities in the Pedersen conductivity layer. Therefore, in all Pedersen conductivity calculations that follow, the background neutral parameters and ion fractions are specified using STIM.

[15] Figure 1 (left) shows two Cassini RSS profiles to illustrate the low-altitude limitations of some of the data. Saturn occultation 058x (top) occurred at −74.1° latitude, near local dusk. Occultation 068n (bottom) occurred at 27.7° latitude, also near dusk. Above ~1500 km, the shapes of the two profiles are roughly similar. Below 1500 km, however, 058x cuts off while 068x continues down to ~800 km altitude. The central panels represent the resulting calculations of Pedersen conductivities, using STIM to specify neutral and ion parameters (treated in section 4). Clearly, where there is no electron density information, the conductivity is also missing, and this results in the Pedersen conductance estimate for the 058x occultation (0.23 mho) being a factor of ~30 smaller than the corresponding estimate for the 068n occultation (7.06 mho). Finally, the panels on the right show the percent of the total height-integrated Pedersen conductivity (i.e., conductance) as a function of altitude. Despite occultation 068n having two electron density peaks of similar magnitude at ~1600 and ~1100 km, the conductivities corresponding to those bumps are quite different, and in fact ~90% of the total conductance estimated from the 068n occultation occurs below 1100 km. Thus, as is well known in terrestrial electrodynamics [*Kelley*, 2009; *Schunk and Nagy*, 2009], Pedersen conductivities at Saturn also peak in the low-altitude ionosphere. When low-altitude electron densities are missing from radio occultation electron density profiles we must discard that occultation from further Pedersen conductance analysis. Six such profiles have been
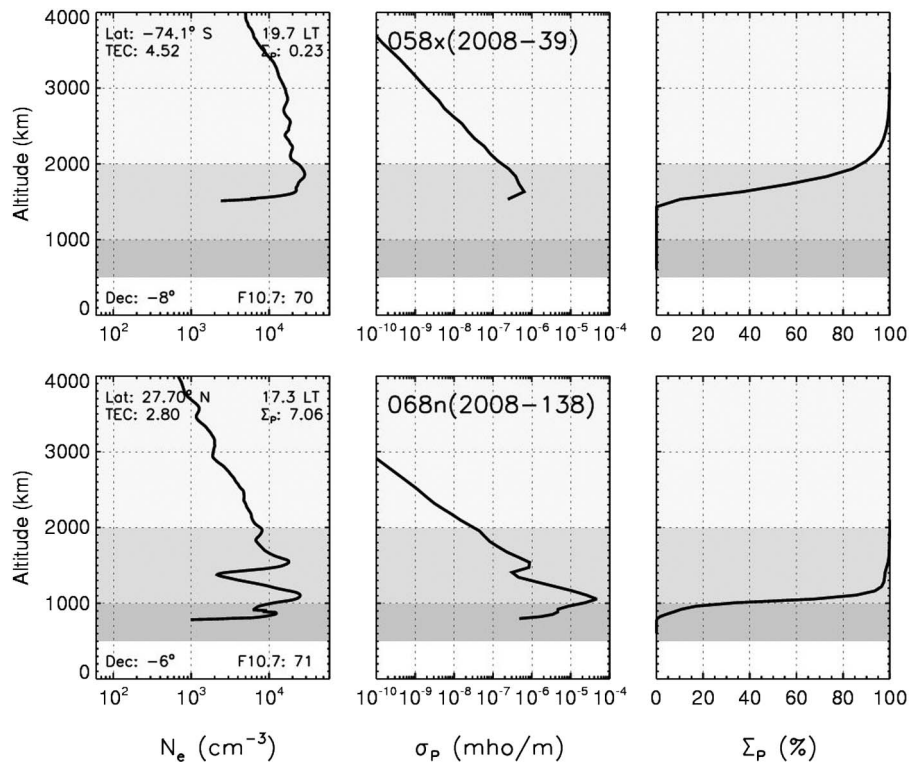
Figure 1. Cassini RSS occultations (top) 058x and (bottom) 068n versus altitude. (left) The parameters shown are electron density, (middle) Pedersen conductivity, and (right) the percentage of the total Pedersen conductance. Electron density profiles are by *Kliore et al.* [2009]; Pedersen calculations use the published RSS electron densities along with STIM-derived neutral and ion densities. The shaded areas indicate the approximate regions of Pedersen conductance generation, with the peak conductivity typically occurring near 1000 km altitude. The darkest region (between 500 and 1000 km altitude) is dominated by heavy hydrocarbon ions, while the middle region (between 1000 and 2000 km) is predicted to be dominated by H^+ and H_3^+ [e.g., see *Moore et al.*, 2009, Figure 1c].

removed from the conductance calculations: 010n, 044n, 046n, 058x, 068x, and 075x, leaving 25 profiles for analysis.

[16] In addition to latitudinal trends in N_{MAX} and Σ_P, we also evaluate trends in the total electron content (TEC). While conductivities are dominated by bottomside structures in $N_e(h)$ profiles, TEC is formed from its integral using fixed lower and upper altitude limits. At Earth, the altitude span typically considered is ~80 to 2000 km, and two thirds of the TEC occurs above h_{MAX}. Thus TEC is more sensitive to structures and processes at higher altitudes. For Saturn, the pressure range of the background GCM discussed above is 0.42 Pa at the bottom to 3.45×10^{-7} Pa at the top, corresponding to an approximate altitude range of 600 to 2300–3000 km (depending on latitude). The majority of Cassini RSS profiles extend far above this altitude range, and therefore the ionospheric module extrapolates the neutral atmosphere to an upper level of 7.42×10^{-11} Pa (or ~4000–5600 km, depending on latitude). This extrapolation assumes an isothermal atmosphere above the GCM boundary and maintains the upper boundary values in the neutral winds. Ionospheric calculations with and without an extrapolated thermosphere agree below the point of extrapolation. TEC values are then calculated for the full pressure range of the ionospheric model by interpolating the Cassini radio occultation profiles onto the STIM altitude grid. This interpolation ensures that an identical pressure range is used to calculate

TEC for each occultation, as the extent in altitude of the Saturn thermosphere varies with latitude. When Cassini $N_e(h)$ profiles do not extend the majority of the pressure range of the model, they are not used in the analysis of TEC trends. Three such profiles fulfill this condition: 009x, 012n, 012x, and thus 28 profiles are used in our analysis of TEC patterns.

3. Results: Electron Densities

3.1. Electron Density Variations With Latitude: N_{MAX} and TEC

[17] The trend in N_{MAX} identified by *Kliore et al.* [2009] is based on averaging the low-latitude (0°–|30°|), mid-latitude (|30°|–|60°|), and high-latitude (>|60°|) electron density profiles. The top panel of Figure 2 presents the individual N_{MAX} values as a function of latitude to demonstrate that the trend holds in both hemispheres. Near Saturn's equator, the dawn/dusk asymmetry in N_{MAX} [*Nagy et al.*, 2006] is also clearly evident, as the dusk values (circles) are all above the dawn values (asterisks). Also shown is a parabolic fit to the Cassini RSS values of the form

$$N_{MAX}(cm^{-3}) = 6400\,cm^{-3} + (45\,cm^{-3}deg^{-1})b$$
$$+ (4.4\,cm^{-3}deg^{-2})b^2, \tag{1}$$
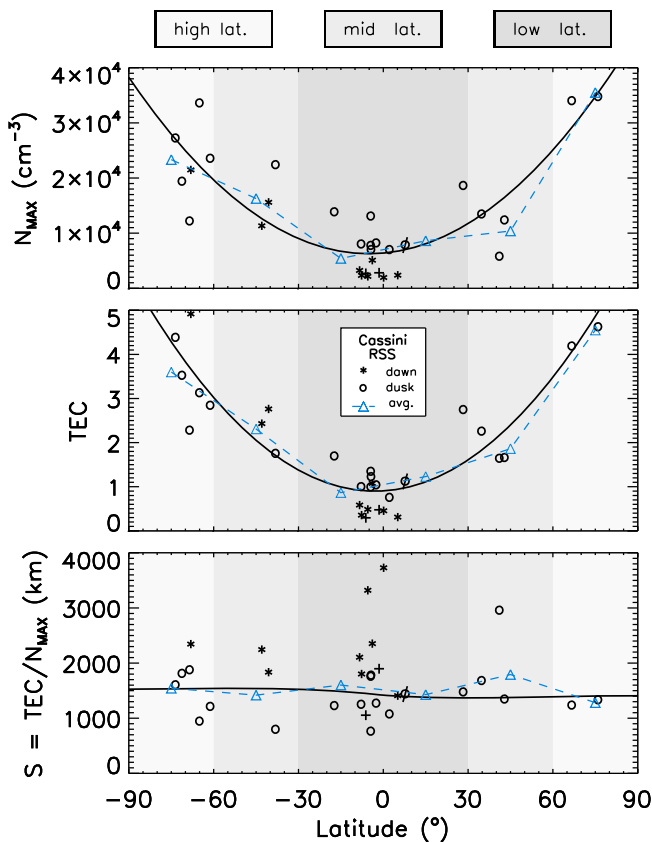
Figure 2. Latitudinal variations of (top) N_{MAX}, (middle) TEC, and (bottom) slab thickness S from the Cassini RSS radio occultation observations [*Kliore et al.*, 2009]. Dawn values are shown as asterisks, dusk values as circles. Degrees of shading, from darkest to lightest, correspond to low-, mid-, and high-latitude regions, respectively. The blue dashed curve tracks the average values for each panel in 30° latitude bins, given by triangles, while solid curves represent parabolic fits to the full data set for N_{MAX} and TEC, and the ratio of those fits for S (see text). For completeness, the three occultations that are not included in the trend analyses due to high-altitude dropouts in electron density (009x, 012n, 012x) are indicated as pluses (dawn) and phi (dusk). (One TEC unit corresponds to a column density of 10^{16} e$^-$ m^{-2}.)

where b is Saturn latitude in degrees and the correlation coefficient is ~0.7 (1.0 would represent a perfect correlation).

[18] For TEC (middle panel), the latitude trend is very similar, although with less scatter. The asymmetry between dawn and dusk values is preserved at equatorial latitudes, but it is reversed at middle and high latitudes, i.e., the three dawn values (asterisks) are above the six nearby dusk values in the southern hemisphere (circles). A reversal of the dawn/dusk asymmetry at high latitude may be an indication of auroral precipitation, which tends to peak in the dawn sector at Saturn [e.g., *Gérard et al.*, 2005]. Again we show a parabolic fit to the data, this time of the form

$$TEC = 0.91 + (3.9 \times 10^{-3} \, \text{deg}^{-1})b + (7 \times 10^{-4} \text{deg}^{-2})b^2,$$

where the correlation coefficient is 0.82. (1 TEC = 10^{12} e$^-$ cm^{-2} = 10^{16} e$^-$ m^{-2}.)

[19] As the average solar declination for the Cassini measurements is −8.5°, one might anticipate that the late summer conditions in the southern hemisphere would show N_{MAX} and TEC values to be higher at southern middle latitudes than in the northern hemisphere, and that is basically the case (see light shaded regions in Figure 2). Yet the overall latitude trend is counter to what would be expected in a basic solar-produced ionosphere, where the larger solar zenith angles at high latitude lead to smaller photoionization rates. Even if we accepted that all of the high-latitude Cassini occultation measurements were augmented by ionization due to auroral precipitation (a possibility that we can neither prove nor disprove, as discussed in section 5), it would remain puzzling that the mid-latitude ionosphere (in both the north and the south) has a higher N_{MAX} than the equatorial ionosphere. Therefore, to reproduce the trends in N_{MAX} and TEC shown in Figure 2, additional latitude-dependent production and/or loss processes are required in the model.

[20] The bottom panel in Figure 2 gives the ratio of peak density to total electron content. This parameter has the unit of length and represents the so-called "equivalent slab thickness S" of an ionosphere. It describes how broad an ionosphere would be if the electron density were everywhere equal to the peak density, and thus serves as an indicator of the overall shape of the ionosphere. There are two quantitative messages from this panel: (1) Saturn's ionosphere has a uniformly broader altitude span at dawn versus dusk at all latitudes, and particularly so near the equator, and (2) the average values of slab thickness in each latitude domain (blue triangles) are very similar (~1500 km). The first message is another aspect of the mix of atomic (H^+) and molecular (H_3^+) ions in Saturn's ionosphere. Just as the recombination of H_3^+ during the nighttime leads to a dawn N_{MAX} value that is lower than the dusk N_{MAX} value, the resulting heightened relative importance of H^+ at dawn, which has a broader altitude distribution than H_3^+ due to its lower mass, gives rise to larger slab thicknesses (S) at dawn. The unusually large dawn values of S at dawn near the equator are another indication of enhanced loss processes at low latitude, as recombination chemistry removes ionization at altitudes near and below h_{MAX}, while ionization in the topside persists.

[21] To gauge how well STIM calculations can reproduce the latitudinal trend observed by Cassini RSS, we performed a series of global ionospheric calculations for "average" Cassini conditions (see section 2.1) over a range of possible H_2 vibrational distributions. Enhanced vibrational populations of H_2 reduce the modeled electron density by exchanging long-lived H^+ ions for short-lived H_3^+ ions [i.e., *Moore et al.*, 2004]. The reaction rate for charge exchange between H^+ and vibrationally excited H_2 at 600 K (i.e., the approximate condition in Saturn's ionosphere) is estimated to be between $(0.6–1.3) \times 10^{-9}$ cm^{-3} s^{-1} [*Huestis*, 2008; see also *Ichihara et al.*, 2000; *Krstić*, 2002; *Krstić et al.*, 2002]; we chose $k_1 = 10^{-9}$ cm^{-3} s^{-1}. We used the approach of *Moses and Bass* [2000] to specify our initial population of vibrationally excited H_2. While this is a simple approximation, it is a reasonable starting point, and the final value depends on how well the model reproduces Cassini observations. In the following, the net reaction rate is given
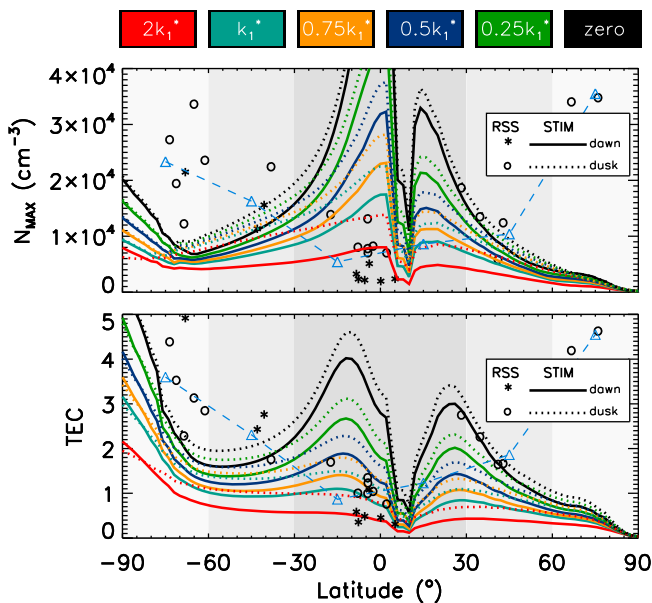
Figure 3. Latitudinal variations of (top) N_{MAX} and (bottom) TEC from the Cassini RSS radio occultation observations [*Kliore et al.*, 2009] and from model calculations. Six different values of the reaction rate between H^+ and vibrationally excited H_2 are identified in the colored rectangles; corresponding STIM calculations are shown for dawn (06 LT) and dusk (18 LT) in solid and dotted lines, respectively. Model calculations do not include any water influx. The sharp decrease in modeled N_{MAX} and TEC near 10° latitude is the result of shadows cast by Saturn's rings on its northern ionosphere for a solar declination of −8.5°.

by $k_1^* = k_1$ [$H_2(\nu \geq 4)$], where [ ] denotes the number density in those vibrational states. Modifications we will make to this rate refer to enhancements or reductions in [$H_2(\nu \geq 4)$], and not to an alteration in the value of k_1.

[22] Figure 3 presents STIM calculations of N_{MAX} (top) and TEC (bottom) for a range of H_2 vibrational distributions and compares them with the Cassini RSS values. As in Figure 2, RSS values are identified by asterisks (dawn) and circles (dusk), with 30° bin averages given by light blue triangles. In addition, six latitudinal variations of the modeled N_{MAX} and TEC are overplotted, representing six variations of the modeled H_2 vibrational distribution: 2 k_1^*, k_1^*, 0.75 k_1^*, 0.5 k_1^*, 0.25 k_1^*, and zero (meaning this reaction is removed). Dawn (06 LT) model results are represented by solid curves; dusk (18 LT) by dotted. Notice the overall solstice pattern with summer conditions in the southern hemisphere. Increases in modeled N_{MAX} and TEC values in the southern polar region are due to those latitudes being bathed in constant sunlight; conversely, the precipitous falloff in N_{MAX} and TEC in the northern polar region is due to those latitudes receiving no solar photons for the modeled season. A sharp decrease is present in the modeled N_{MAX} and TEC near 10° latitude; this is the result of the shadow cast by Saturn's rings on its northern ionosphere for a solar declination of −8.5°. Within this context, it is interesting to note that only one dawn observation might have occurred near a ring shadowing location, and it has the overall lowest TEC value.

[23] It is apparent from Figure 3 that the model predicts a trend that is nearly opposite to that observed by Cassini: Model N_{MAX} and TEC values are too large near the equator and too small elsewhere. No model simulation comes close to reproducing the high northern latitude Cassini RSS profiles, meaning that additional sources of ionization are required there. There is a similar discrepancy, at least in N_{MAX}, at high southern latitudes. Model simulations are nearly all too large at equatorial latitudes (outside the ring-shadowed region), perhaps indicating a missing low-latitude loss process. Thus, for STIM to reproduce the latitudinal trends observed by Cassini, additional production and loss processes must be introduced that also vary with latitude. If a missing process is one of production, auroral precipitation could provide a high-latitude ionization source, although most of the Cassini RSS profiles appear to be outside of the statistical main auroral oval [e.g., *Badman et al.*, 2006] (we address the auroral issue more completely in section 5). If the necessary model adjustment relates to loss, there are (at least) two candidate processes to consider. The population of vibrationally excited H_2 could be expected to vary with latitude and local time; its variation is accounted for here only by the six colored model runs in Figure 3. Water influxes might also be expected to vary with latitude, with a maximum in Saturn's equatorial region [*Jurac and Richardson*, 2005; *Bjoraker et al.*, 2008]; however, there is no consensus on a latitudinally varying water influx. For example, *Moses et al.* [2000] argue for a global influx of 1.5×10^6 cm^{-2} s^{-1}. Following the methods described by *Moore et al.* [2006], we consider a series of simulations that allow a water influx peaked at Saturn's equator. These simulations evaluate a Gaussian water influx centered on the equator with a peak value of $(0.1–1) \times 10^7$ cm^{-2} s^{-1} and a range of full width half maxima from 2°–180° (in addition to a latitudinally invariant water influx).

[24] The patterns shown in Figure 4 are the best fit to the Cassini observations following many trials using STIM with different loss processes. Thus, the background conditions are identical to the simulations in Figure 3, except that now the reaction rate between H^+ and vibrationally excited H_2 has been fixed at 25% of the k_1^* value given earlier (hence the green lines; see Figure 3), and a latitudinally varying water influx of the form $\phi = 5 \times 10^6 \, e^{-b^2/2\sigma^2}$ H_2O molecules cm^{-2} s^{-1} has been introduced, where b is Saturn latitude in degrees and the variance σ is 10°, corresponding to a full width half max of ~23.5°. This is essentially identical to the fit for the low-latitude ionosphere derived previously [*Moore et al.*, 2006]. Model/data agreement in N_{MAX} is good to within a factor of two for low and middle latitudes (darker shaded areas) and a factor of three at high latitudes in the southern summer hemisphere. Agreement in TEC is approximately similar, although the model does a better job at high latitudes in the southern hemisphere for TEC than it does for N_{MAX}. The largest model/data discrepancies occur in the high-latitude region of the northern winter hemisphere, where the model underpredicts N_{MAX} by nearly a factor of 20 and TEC by roughly a factor of nine.

3.2. Effects of Solar Cycle and Solar Declination (Seasonal) Conditions

[25] We cannot dismiss the possibility that the model may be able to reproduce the N_{MAX} and TEC values observed by
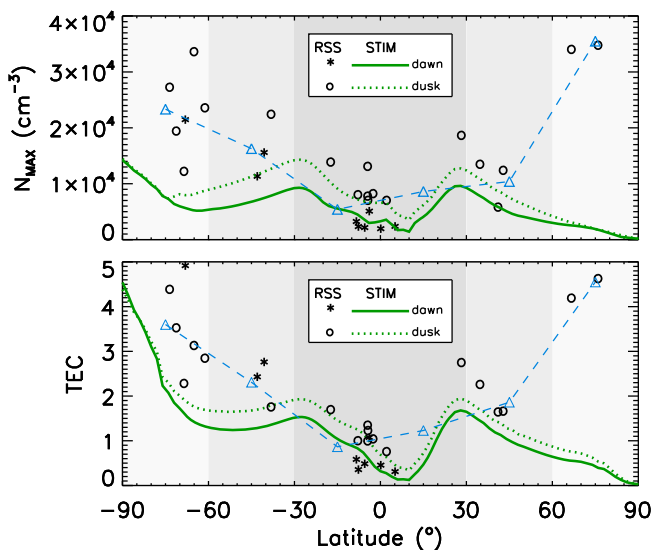
Figure 4. Latitudinal variations of (top) N_{MAX} and (bottom) TEC from the Cassini RSS radio occultation observations [*Kliore et al.*, 2009] and from the model simulation that comes nearest to reproducing the observed trends in N_{MAX} and TEC. Conditions for this model simulation are: effective reaction rate between H^+ and vibrationally excited H_2 of $k = 0.25\ k_1^*$ and a latitudinally varying water influx of the form $\phi = 5 \times 10^6\ e^{-b^2/2\sigma^2}$ H_2O molecules $cm^{-2}\ s^{-1}$, where b is Saturn latitude in degrees and the variance σ is 10°, corresponding to a full width half max of ~23.5°.

Cassini RSS based on Figure 4 alone simply because background conditions changed during the period of observations. During the time span over which the 31 Cassini radio occultation measurements were made, Saturn's solar declination changed from −24.5° to −6° and solar F10.7 indices varied between 116 and 66 units. Therefore, it will be useful to demonstrate the full range of the model predictions by considering simulations for the multiyear variations of Saturn seasons and solar irradiances. Saturn's axial tilt is 26.73° and the first Cassini radio occultation occurred very close to southern summer solstice. To distinguish from the previous model simulations that used −8.5° as a solar declination, we will consider Saturn equinox as the other seasonal boundary. Finally, although clearly no Cassini radio occultation occurred near solar maximum, it will be useful to compare solar minimum and solar maximum conditions to describe the full range of possible solar-produced model values for N_{MAX} and TEC.

[26] First, we consider the effect of a variation in solar flux on Saturn's latitudinal trends. Figure 5 shows model simulations for Saturn equinox during solar minimum and solar maximum time periods. We again use the TIMED/SEE solar fluxes, extrapolated to Saturn. Solar minimum is represented by the 15 March 2008 flux (F10.7 = 70); solar maximum is represented by the 20 October 2002 flux (F10.7 = 180). The range between solar minimum dawn values (solid yellow line) and solar maximum dawn values (solid red line) is highlighted yellow, while the range between solar minimum dusk values (dotted yellow line) and solar maximum dusk values (solid red line) is shaded red. The area of overlap is shown in orange. Any N_{MAX} or TEC values outside of the

colored areas are not possible to reproduce with STIM, within this range of solar flux, at least for this particular set of model conditions. The only significant model/data discrepancies in Figure 5 are again at high latitudes.

[27] Figure 6 has the same format as Figure 5, except for southern summer solstice conditions (i.e., the solar declination is −26.73°). The increase in solar illumination in the southern hemisphere increases the modeled electron densities; there is a corresponding decrease in electron densities in the northern hemisphere. The good agreement between the model and the Cassini observations in the southern hemisphere indicate that it is possible to explain the trend of increasing N_{MAX} and TEC values with latitude in the summer hemisphere. It is important to note, however, that the six Cassini radio occultations at latitudes between −60° and −90° occurred for solar declinations between ~9° and −6°, i.e., much nearer to equinox than to southern summer (−26.73°).

[28] To demonstrate the effect of seasonal changes during a fixed phase of the solar cycle on modeled electron densities, Figure 7 presents a comparison of N_{MAX} and TEC for southern summer solstice and equinox at Saturn during solar
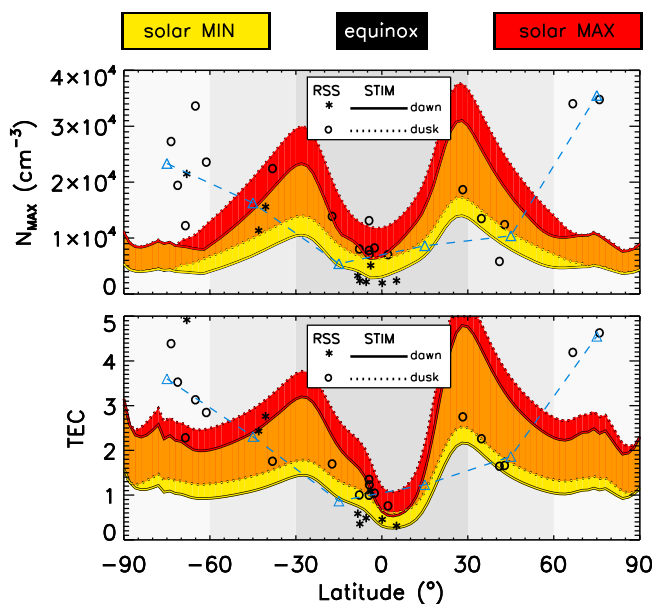
Figure 5. Latitudinal variations of (top) N_{MAX} and (bottom) TEC from the Cassini RSS radio occultation observations [*Kliore et al.*, 2009] and from model calculations. Two model simulations are shown: one for solar minimum conditions and one for solar maximum conditions, both at Saturn equinox. On the basis of the best match from Figure 4, these simulations use an effective reaction rate between H^+ and vibrationally excited H_2 of $k = 0.25\ k_1^*$ and a latitudinally varying water influx of the form $\phi = 5 \times 10^6\ e^{-b^2/2\sigma^2}$ H_2O molecules $cm^{-2}\ s^{-1}$, where b is Saturn latitude and the variance σ is 10°, corresponding to a full width half max of ~23.5°. The area between the dawn solar minimum values (solid yellow line) and the dusk solar minimum values (solid red line) is yellow, while the area between the dusk solar minimum values (dotted yellow line) and the dusk solar maximum values (dotted red line) is red. Areas where these two regions overlap are orange.
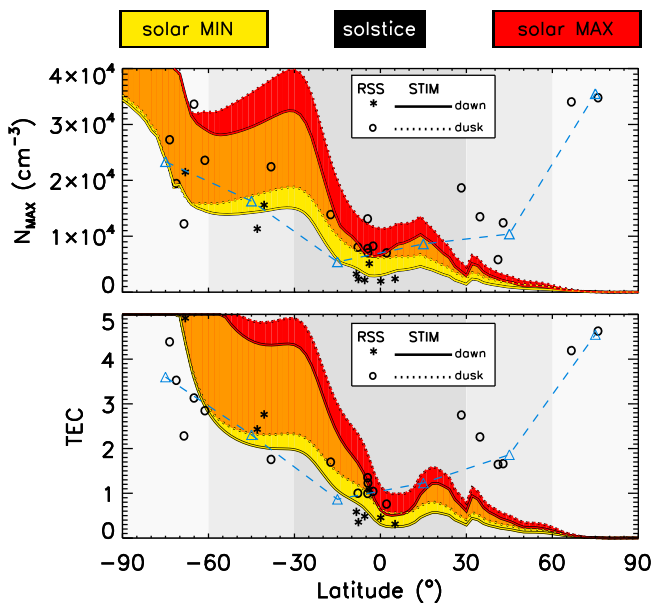
Figure 6. Same as Figure 5 except for Saturn's southern summer solstice rather than equinox.

minimum conditions. In Figure 7, the model is able to approximately reproduce the Cassini observations for all latitudes except high northern latitudes, which the model can only reproduce to within factors of six and three for N_{MAX} and TEC, respectively, no matter the Saturn season. The high northern latitude occultations, 044n and 072x, are from 75.4° and 66.1° latitude. Both occultations exhibit a double-peak structure with a significant valley in between, although at very different altitudes. Electron density peaks for occultation 044n peaks occur at ~1800 and ~2800 km, while those of occultation 072x are at ~900 and ~2400 km. The model's inability to come close to reproducing the electron densities of 044n and 072x is indicative of a missing source of ionization, as nearly all of the unconstrained standard chemical losses (i.e., charge exchange between H^+ and H_2O and/or H_2*) have been removed from the simulations already. Occultation 044n is at the right latitude to be within the main auroral oval at 75.4° latitude, but 072x seems to be well outside at 66.1° latitude.

[29] In summary, we have adopted a broad simulation approach to the full set of Cassini RSS observations. When treated as independent data points, it is always possible to find a case-by-case set of model input parameters that provide a reasonable representation of the data. Here, we offered a more comprehensive approach to the patterns those observations suggest. We fixed the reaction rate for H_2-vibrational loss on a global basis and the water influx for loss at equatorial and low latitudes. Within this framework, the message that emerges is that solar production and photochemistry account for the broad seasonal latitude trends observed from equatorial to middle latitudes in the total amount of plasma present (i.e., TEC), as well as in the peak values of electron density (N_{MAX}). Shortfalls in production from subauroral to high latitudes are probably due to the noninclusion of magnetospheric sources (particle precipitation) in the model, a topic to be addressed in section 5. Prior to that, we present an additional assessment of the $N_e(h)$

profiles that is related directly to magnetosphere-ionosphere coupling.

4. Results: Pedersen Conductance

[30] Pedersen conductivity is given by the expression

$$\sigma_P = \sum_i \left(\frac{n_i e_i^2}{m_i}\right)\frac{\nu_{in}}{\nu_{in}^2 + \omega_i^2} + \left(\frac{N_e e^2}{m_e}\right)\frac{\nu_{en}}{\nu_{en}^2 + \omega_e^2}, \quad (2)$$

where n_i/N_e is the ion/electron number density, e_i/e_e is the ion/electron charge, m_i/m_e is the ion/electron mass, ν_{in}/ν_{en} is the ion/electron-neutral collision frequency, and ω_i/ω_e is the ion/electron gyro frequency [*Schunk and Nagy*, 2009]. Pedersen conductance Σ_P then is simply the integral of the computed conductivities over altitude $\Sigma_P = \int_{bottom}^{top} \sigma_P dz$. Cassini radio occultations provide the total electron density N_e as a function of altitude, from which we can constrain the total ion density Σn_i, assuming positive ions. In the terrestrial ionosphere, at and above E-layer altitudes, the ratio between ν_{en} and ω_e is extremely small, meaning electrons contribute little to the Pedersen conductivity. This holds true at Saturn as well, as conductivities (such as in Figure 1) are dominated by the ion term in equation (1). STIM is used to specify the background neutral atmosphere to calculate ion-neutral collision frequencies. The remaining unknowns then are the relative ion fractions that make up the observed electron density. Ion fractions are taken from our modeled ionosphere and applied to the observed electron density profiles, after having first interpolated the Cassini measurements onto an identical pressure grid. In this way, an exact match between modeled and observed $N_e(h)$ profiles is not required (i.e., the low-altitude ionic patterns are the more relevant concerns). Put another way, Cassini RSS provides
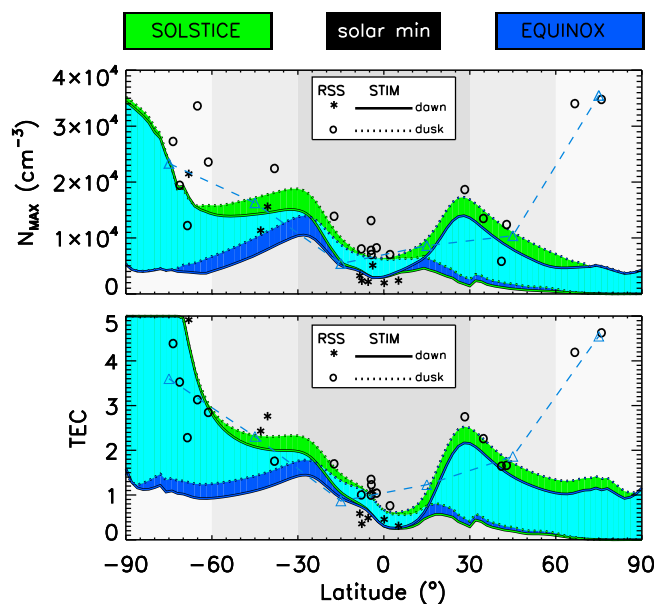
Figure 7. Same as Figure 5 except rather than comparing solar minimum and solar maximum conditions, model simulations are for southern summer solstice and equinox, both during solar minimum.
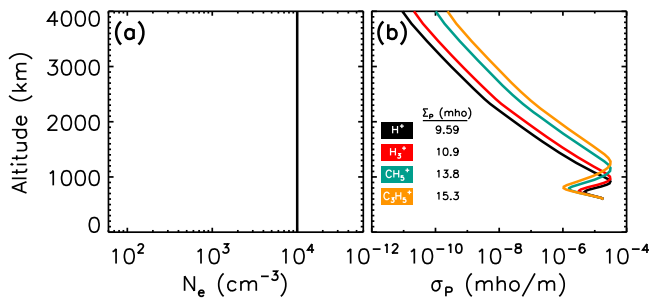
Figure 8. (a) Idealized electron density profile of 10^4 cm^{-3}, constant with altitude. (b) Resulting Pedersen conductivities when the ion distribution is assumed to be entirely H$^+$ (black), H$_3^+$ (red), CH$_5^+$ (blue), or C$_3$H$_5^+$ (orange).

the total electron density and STIM provides the relative ion fractions.

[31] It is important to note that Pedersen conductivities are functions of ion mass. As shown in Figure 1, conductivities peak near 1000 km in the ionosphere, which is thought to be a key transition region between the main ionospheric peak dominated by H$^+$ and H$_3^+$ ions and a hydrocarbon ledge dominated by complex, heavy hydrocarbon ions, predominately C$_3$H$_5^+$ [*Moses and Bass*, 2000]. The ionospheric models considered here do not include the full hydrocarbon photochemistry with its hundreds of reactions and more than 30 hydrocarbon ion species; instead, we consider only a minimal set of reactions, primarily as a sink for H$^+$ and H$_3^+$ [*Moore et al.*, 2004]. While we are able to reproduce the electron density of the hydrocarbon ledge fairly well [*Moore et al.*, 2008] when compared with more complete calculations [*Moses and Bass*, 2000], the heaviest ion our scheme includes is CH$_5^+$, two carbon atoms lighter than the major hydrocarbon of the Moses and Bass scheme, C$_3$H$_5^+$.
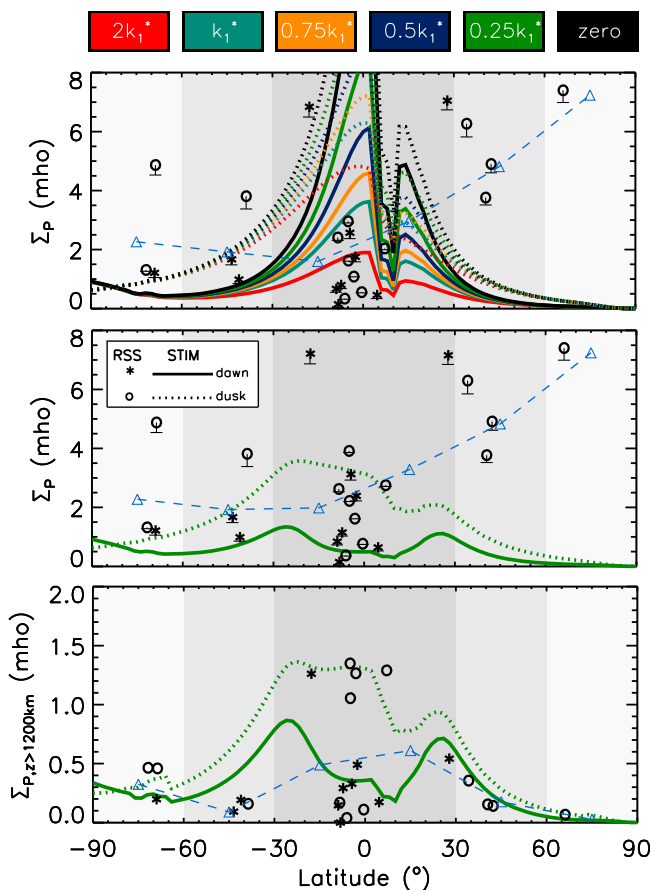
[32] In an attempt to quantify the degree to which calculated Pedersen conductances are affected by not considering C$_3$H$_5^+$ ion chemistry, Figure 8 presents a series of trial calculations of Pedersen conductivity. Figure 8a shows the electron density profile, which is taken to be 10^4 cm^{-3} and constant with altitude. This is clearly a nonphysical assumption, but it is useful for demonstrating the altitude regime of the Pedersen conductivity layer at Saturn. Four resulting profiles of Pedersen conductivity are plotted in Figure 8b. In each case, the assumption is made that the entire N$_e$(h) profile from Figure 8a is made up entirely of a single species of ion: H$^+$ (black), H$_3^+$ (red), CH$_5^+$ (blue), or C$_3$H$_5^+$ (orange). The first point to note is that, despite the electron density being constant with altitude, Pedersen conductivities peak between ~900 and ~1300 km, depending on ion species. Second, because of the difference in the ratios between ion-neutral collision frequencies and ion gyro frequencies, each ion peaks at a slightly different altitude. The Pedersen conductances given in Figure 8b are based on a nonphysical electron density profile, but help to gauge the degree to which we underestimate the conductances observed by Cassini. For example, in the extreme case in which all of the ions in Saturn's ionosphere are assumed to be C$_3$H$_5^+$, our calculations, which only consider hydrocarbons up to CH$_5^+$, would be off by 1.5 mho. However, it is slightly more complicated than that, as the major ions above 1000 km will most likely not be hydrocarbon

ions [e.g., *Moses and Bass*, 2000; *Moore et al.*, 2008], meaning the conductivity peaks between 1100 and 1300 km shown in Figure 8b would be reduced in magnitude. A more realistic Pedersen conductivity profile would be a curve that falls somewhere between the red and black lines above 1000 km and transitions to the orange line below 1000 km. For such a case, the difference in area between the blue and orange curves below 1000 km describes the error that would be expected from the model's neglect of the full hydrocarbon chemistry. On the basis of Figure 8, this error is calculated to be an overestimate of the Pedersen conductance by ~0.6 mho. For the majority of Cassini radio occultations, this error would be smaller, as the hydrocarbon ledge has a more typical density of ~10^3 cm^{-3} rather than the 10^4 cm^{-3} considered here. In fact, the error scales with ion density within the hydrocarbon ion regime, as $\sigma_p \propto n_i$. An analysis identical to the one that leads to an estimate of 0.6 mho as the error, except using 10^3 cm^{-3} in place of 10^4 cm^{-3} for the electron density, would lead to an error estimate of 0.06 mho.

[33] Figure 9 presents calculations of the ionospheric Pedersen conductance as a function of latitude based on Cassini RSS radio occultation profiles of electron density and model calculations. As with electron densities, we consider a series of simulations that utilize averaged solar flux and solar declination conditions (see section 2.1). The top panel shows the results for a range of vibrational distributions of H$_2$, with zero water influx. The center panel shows the model simulation that comes closest to reproducing the observed trend in conductance; these model conditions are identical to those plotted in Figure 4. Pedersen conductances for the Cassini RSS observations are calculated using the measured N$_e$(h) profiles combined with the modeled neutral densities and ion fractions. On the basis of the preceding error analysis, it is estimated that the resulting Cassini RSS conductances are roughly 0.06–0.6 mho too large.

[34] As shown in Figure 9, the model is able to reproduce a very rough approximation to the Cassini-derived trend in conductance; however, remain significant discrepancies remain, particularly in the northern winter hemisphere. The poorest model estimate is for occultation 072x at 66.1° latitude, where the model is more than a factor of 14 too low. This is the same occultation that proved impossible to reproduce in Figures 5–7 using variations in Saturn season and/or solar flux, reinforcing the argument that an additional source of high-latitude ionization is required here, probably auroral. Just as in Figure 4, the model would overestimate equatorial conductances without incorporating an additional loss process (e.g., water influx) at low latitudes. Other mid- and high-latitude model/data discrepancies in the middle panel indicate that the modeled ionosphere is underestimating the observed electron densities in the Pedersen conductance layer.

[35] Secondary ionization by suprathermal electrons plays an important role in modulating the Saturn ionosphere in this altitude regime, accounting for approximately 10 out of every 11 ions produced at 800 km [*Galand et al.*, 2009]. The model calculations here incorporate a parameterization of the secondary ionization rate that was derived for different background conditions at Saturn [*Moore et al.*, 2009]. However, this is also the region of the ionosphere with the

highest degree of variability and sharp vertical structuring [*Nagy et al.*, 2006; *Kliore et al.*, 2009], neither of which are well explained at present. Note also that by comparing the model's calculated conductances with the Cassini-derived conductances we are in effect comparing the modeled low-altitude electron densities with the observed low-altitude electron densities, as both calculations utilize the same background neutral atmosphere. Therefore, the model/data discrepancies in Figure 9 are indicative of the model's inability to reproduce these sharp electron density layers, which would require additional physics in order to adequately model (e.g., gravity wave breaking [*Matcheva et al.*, 2001]). Until the variability and electron layers are well understood, it is difficult to point to any conclusive limitations within the model that would lead to the present disagreements with Cassini observations.

[36] The bottom panel in Figure 9 offers another way to see how the bottomside ionosphere dominates conductance by plotting the observed and modeled results that come from using only values above 1200 km altitude. The values coming from observations generally fall within the envelopes of the model, stressing that solar-produced effects versus latitude are the main drivers of these topside contributions to total conductance.

[37] Finally, we note that the modeled Pedersen conductances shown here are much smaller than those originally estimated by *Moore et al.* [2004]. An error in the specification of the magnetic field magnitude lead to those values being too large by nearly a factor of 8, and therefore, these new estimates that use the SPV magnetic field take precedence.

5. Discussion and Summary

[38] Initial results from STIM dealt with latitude variations predicted by photochemistry only, including localized modifications due to ring shadowing of solar irradiances [*Moore et al.*, 2004; *Mendillo et al.*, 2005]. Here we present the first study of latitudinal variations in Saturn's ionosphere constrained by measurements over a broad range of latitudes. Cassini RSS radio occultation observations of electron density have now demonstrated an electron density trend (tracked here using N_{MAX} and TEC) that increases with latitude, with a minimum at Saturn's equator [*Kliore et al.*, 2009]. All previous theoretical estimates, based on solar photons being the only ionization source process, predicted a trend nearly opposite to the observed one [e.g., *Moore et al.*, 2004]. The initial set of Cassini profiles were at equatorial latitudes [*Nagy et al.*, 2006], and successful simulations required a low-latitude enhancement of photochemical loss rates. This enhancement was provided by the implementation of previously postulated influxes of water [see *Moore et al.*, 2006, and references therein].

[39] Now that a more complete set of Cassini profiles versus latitude is available, we find that model calculations are again able to reproduce the observed trend at low and middle latitudes when an additional latitude-dependent loss process is introduced. The water influx found to best match observations here takes the form $\phi = 5 \times 10^6 e^{-b/2\sigma^2}$ H_2O molecules cm^{-2} s^{-1}, where b is Saturn latitude in degrees and the variance σ is 10°, corresponding to a full width half max of ~23.5° latitude. Other water influxes with magnitudes

Figure 9. Latitudinal variations of Pedersen conductance (Σ_P) estimated from the Cassini RSS radio occultation observations [*Kliore et al.*, 2009] and from model calculations. Dusk and dawn Cassini-derived conductances are shown as circles and asterisks, respectively. Error bars due to the model's neglect of $C_3H_5^+$ ion chemistry are also shown; these errors are calculated by scaling the 0.6 mho error estimated in the text using the mean measured electron densities between 700 and 1100 km. Blue triangles and dashed lines track Cassini conductances averaged in 30° latitude bins. (top) Six different values of the reaction rate between H^+ and vibrationally excited H_2 are identified in the colored rectangles above; corresponding STIM calculations are shown for dawn (06 LT) and dusk (18 LT) in solid and dotted lines, respectively. Model calculations in the top panel do not include any water influx. (middle) The model simulation that comes nearest to reproducing the observed trend in Σ_P. Conditions for this model simulation are identical to those in Figure 4, namely: effective reaction rate between H^+ and vibrationally excited H_2 of $k = 0.25 k_1^*$ and a latitudinally varying water influx of the form $\phi = 5 \times 10^6 e^{-b^2/2\sigma^2}$ H_2O molecules cm^{-2} s^{-1}, where b is Saturn latitude in degrees and the variance σ is 10°, corresponding to a full width half max of ~23.5°. (bottom) Pedersen conductance values for Cassini and STIM calculated using only electron densities above 1200 km altitude.

down to 1×10^6 cm^{-2} s^{-1} would produce nearly as good as a match, but still require a latitude-dependent influx. Current observational constraints on neutral water influx at Saturn are conflicted in whether the modeled water influx is realistic. For example, *Moses et al.* [2000] argue for a global influx based on Infrared Space Observatory observations [*Feuchtgruber et al.*, 1997], while the HST observations in the UV by *Prangé et al.* [2006] are consistent with a localized mid-latitude water influx, and *Bjoraker et al.* [2008] observed a latitudinal trend similar to the one modeled here using Cassini's composite infrared spectrometer.

[40] Regardless of the assumed water influx, high-latitude model/data discrepancies remain. Emission from Saturn's auroral oval is observed between ~70°–90° latitude in the UV [e.g., *Clarke et al.*, 2005; *Nichols et al.*, 2009]. Additionally, a secondary oval, roughly 25% as bright as the main oval and equatorward of the main oval, has been observed in the IR [*Stallard et al.*, 2008]. Statistically, the southern auroral oval is ~2° wide, centered at −75° latitude, although there is also significant variability in the emission pattern with local time [*Badman et al.*, 2006]. Three Cassini RSS observations are at latitudes >|70|°, and one within the −74° to −76° southern auroral oval window, 058x [see Table 1 of *Kliore et al.*, 2009]. The 044n observation is also within the statistical northern auroral oval, assuming axisymmetry between Saturn's rotational and magnetic axes, although there is some indication of a ~2° offset of Saturn's southern auroral oval from its rotation axis [*Nichols et al.*, 2008]. Ultraviolet images of Saturn's southern aurora were obtained by the Hubble Space Telescope approximately 12 h before and 14 h after the Cassini 058x occultation (J.T. Clarke, private communication, 2009). An examination of the preceding and following HST images, however, reveals the 058x occultation to have occurred in a particularly quiescent portion of the dusk polar ionosphere. Auroral emission is clearly observable in the dawn sector of the HST images, while the dusk sector is indistinguishable from the background disc emission (an asymmetry common to Saturn aurora, e.g., *Gérard et al.* [2005]). Unfortunately, no other images from HST, or, indeed, from any other Saturn auroral data set (such as the Cassini visual and infrared mapping spectrometer and Ultraviolet Imaging Spectrograph Subsystem instruments) are taken within 1 day of the remaining RSS occultations. Therefore, we cannot state with certainty whether any Cassini RSS occultations occurred in regions of enhanced auroral precipitation. If auroral precipitation is the cause of the additional ionization needed by the model to reproduce the observed high-latitude electron densities, then there must be precipitation outside of the main auroral oval (and at latitudes down to at least |60|°) and it must lead to emission too weak to have been observed previously.

[41] Ionospheric Pedersen conductances are also calculated from Cassini RSS observations for the first time, using model calculations to specify the background atmosphere and ion fractions. The resulting Cassini-derived high-latitude conductances range from 1.11 to 7.4 mho, with an average value of nearly 4 mho. This average is in agreement with the 4 mho proposed for auroral latitudes by *Cowley et al.* [2008]. Mid-latitude Cassini-derived conductances range from 0.88 to 6.30 mho, with an average of just over 4 mho, while low-latitude conductances were between 0.36 and 7.11 mho, with an average of ~2.5 mho. Model simulations were able to reproduce the observed trend in Pedersen conductance only roughly and do particularly poorly at middle and high latitudes, reinforcing the need for additional ionization sources within the model there. The comparison between modeled and observed conductances is additionally hampered by the nature of the Saturn ionosphere at the Pedersen layer, near ~1000 km, which is extremely variable and has a high degree of poorly understood sharp ionospheric layers.

[42] Although it cannot be certain whether any of the Cassini radio occultations studied here were affected by ionization due to auroral precipitation, it seems the most likely explanation for the high-latitude model/data discrepancies. Future studies will investigate this additional ionization source. Preliminary STIM studies have shown auroral conductances to significantly affect Pedersen currents, which deposit thermal energy in the polar regions via Joule heating. Thus, polar temperature measurements should pose additional constraints to the auroral conductances via their effects on Saturn's theremosphere. In addition, Saturn's poorly sampled low-altitude ionosphere, where multipath propagation issues frequently interfere with radio occultation analysis, could benefit from a renewed focus. It is an important transition region between Saturn's "main" ionosphere above and complex hydrocarbon regime below and accounts for the majority of the ionospheric Pedersen conductance.

References

Atreya, S. K., and T. M. Donahue (1975), Ionospheric models of Saturn, Uranus, and Neptune, *Icarus*, *24*, 358–362.

Atreya, S. K., J. H. Waite, T. M. Donahue, A. F. Nagy, and J. C. McConnell (1984), Theory, measurements and models of the upper atmosphere and ionosphere of Saturn, in *Saturn*, edited by E. Gehrels, pp. 239–277, Univ. of Ariz. Press, Tucson, Ariz.

Badman, S. V., S. W. H. Cowley, J.-C. Gérard, and D. Grodent (2006), A statistical analysis of the location and width of Saturn's southern auroras, *Ann. Geophys.*, *24*, 3533–3545.

Bjoraker, G. L., R. K. Achterberg, A. A. Simon-Miller, R. C. Carlson, and D. E. Jennings (2008), CIRS observations of H_2O vapor in stratosphere, paper presented at Saturn After Cassini-Huygens Meeting, London, U. K.

Bunce, E. J., S. W. H. Cowley, and J. A. Wild (2003), Azimuthal magnetic fields in Saturn's magnetosphere: Effects associated with plasma subcorotation and the magnetopause-tail current system, *Ann. Geophys.*, *21*, 1709–1722.

Capone, L. A., R. C. Whitten, S. S. Prasad, and J. Dubach (1977), The ionospheres of Saturn, Uranus, and Neptune, *Astrophys. J.*, *215*, 977–983.

Cheng, A. F., and J. H. Waite Jr. (1988), Corotation lag of Saturn's magnetosphere: Global ionospheric conductivities revisited, *J. Geophys. Res.*, *93*, 4107–4109.

Clarke, J. T., et al. (2005), Morphological differences between Saturn's ultraviolet aurorae and those of Earth and Jupiter, *Nature*, *433*, 717–719.

Connerney, J. E. P., and J. H. Waite Jr. (1984), New model of Saturn's ionosphere with an influx of water from the rings, *Nature*, *312*, 136–138.

Connerney, J. E. P., M. H. Acuña, and N. F. Ness (1983), Currents in Saturn's magnetosphere, *J. Geophys. Res.*, *88*, 8779–8789.

Cowley, S. W. H., E. J. Bunce, and R. Prange (2004), Saturn's polar ionospheric flows and their relation to the main auroral oval, *Ann. Geophys.*, *22*, 1379–1394.

Cowley, S. W. H., C. S. Arridge, E. J. Bunce, J. T. Clarke, A. J. Coates, M. K. Dougherty, D. Grodent, J. D. Nichols, and D. L. Talboys (2008), Auroral current systems in Saturn's magnetosphere: comparison of theoretical models with Cassini and HST observations, *Ann. Geophys.*, *26*, 2613–2630.

Davis, L., Jr., and E. J. Smith (1990), A model of Saturn's magnetic field based on all available data, *J. Geophys. Res.*, *95*, 15,257–15,261.

Feuchtgruber, H., E. Lellouch, T. de Graauw, B. Bézard, T. Encrenaz, and M. Griffin (1997), External supply of oxygen to the atmospheres of the giant planets, *Nature*, *389*, 159–162.

Galand, M., L. Moore, B. Charnay, I. Mueller-Wodarg, and M. Mendillo (2009), Solar primary and secondary ionization at Saturn, *J. Geophys. Res.*, *114*, A06313, doi:10.1029/2008JA013981.

Gérard, J. C., E. J. Bunce, D. Grodent, S. W. H. Cowley, J. T. Clarke, and S. V. Badman (2005), Signature of Saturn's auroral cusp: Simultaneous Hubble Space Telescope FUV observations and upstream solar wind monitoring, *J. Geophys. Res.*, *110*, A11201, doi:10.1029/2005JA011084.

Hallett, J. T., D. E. Shemansky, and X. Liu (2005), A rotational-level hydrogen physical chemistry model for general astrophysical application, *Astrophys. J.*, *624*, 448–461.

Huestis, D. L. (2008), Hydrogen collisions in planetary atmospheres, ionospheres, and magnetospheres, *Planet. Space Sci.*, *56*, 1733–1743.

Ichihara, A., O. Iwamoto, and R. K. Janev (2000), Cross sections for the reaction $H^+ + H_2$ ($v = 0$–14) $\rightarrow H + H_2^+$ at low collision energies, *J. Phys. B At. Mol. Opt. Phys.*, *33*, 4747–4758.

Jurac, S., and J. D. Richardson (2005), A self-consistent model of plasma and neutrals at Saturn: Neutral cloud morphology, *J. Geophys. Res.*, *110*, A09220, doi:10.1029/2004JA010635.

Kelley, M. C. (2009), *The Earth's Ionosphere: Plasma Physics and Electrodynamics*, 2nd ed., 577 pp., Academic, San Diego, Calif.

Kliore, A. J., G. F. Lindal, I. R. Patel, D. N. Sweetnam, and H. B. Hotz (1980a), Vertical structure of the ionosphere and upper neutral atmosphere of Saturn from the Pioneer radio occultation, *Science*, *207*, 446–449.

Kliore, A. J., I. R. Patel, G. F. Lindal, D. M. Sweetnam, H. B. Hotz, J. H. Waite Jr., and T. R. McDonough (1980b), Structure of the ionosphere and atmosphere of Saturn from Pioneer 11 radio occultations, *J. Geophys. Res.*, *85*, 5857–5870.

Kliore, A. J., et al. (2004), Cassini radio science, *Space Sci. Rev.*, *115*, 1–70.

Kliore, A. J., A. F. Nagy, E. A. Marouf, A. Anabtawi, E. Barbinis, D. U. Fleischman, and D. S. Kahan (2009), Midlatitude and high-latitude electron density profiles in the ionosphere of Saturn obtained by Cassini radio occultation observations, *J. Geophys. Res.*, *114*, A04315, doi:10.1029/2008JA013900.

Krstić, P. S. (2002), Inelastic processes from vibrationally excited states in slow $H^+ + H_2$ and $H + H_2^+$ collisions: Excitations and charge transfer, *Phys. Rev. A*, *66*, 042717.

Krstić, P. S., D. R. Schultz, and R. K. Janev (2002), Charge transfer processes in slow collisions of protons with vibrationally excited hydrogen molecules, *Phys. Scr. T*, *96*, 61–71.

Lindal, G. F., D. N. Sweetnam, and V. R. Eshleman (1985), The atmosphere of Saturn—An analysis of the Voyager radio occultation measurements, *Astron. J.*, *90*, 1136–1146.

Majeed, T., and J. C. McConnell (1991), The upper ionospheres of Jupiter and Saturn, *Planet. Space Sci.*, *39*, 1715–1732.

Majeed, T., and J. C. McConnell (1996), Voyager electron density measurements on Saturn: Analysis with a time dependent ionospheric model, *J. Geophys. Res.*, *101*, 7589–7598, doi:10.1029/96JE00115.

Matcheva, K. I., D. F. Strobel, and F. M. Flasar (2001), Interaction of gravity waves with ionospheric plasma: implications for Jupiter's ionosphere, *Icarus*, *152*, 347–365.

McElroy, M. B. (1973), The ionospheres of the major planets, *Space Sci. Rev.*, *14*, 460–473.

Melin, H., S. Miller, T. Stallard, L. M. Trafton, and T. R. Geballe (2007), Variability in the H_3^+ emission of Saturn: Consequences for ionization rates and temperature, *Icarus*, *186*, 234–241.

Mendillo, M., L. Moore, J. Clarke, I. Mueller-Wodarg, W. S. Kurth, and M. L. Kaiser (2005), Effects of ring shadowing on the detection of electrostatic discharges at Saturn, *Geophys. Res. Lett.*, *32*, L05107, doi:10.1029/2004GL021934.

Moore, L., and M. Mendillo (2007), Are depletions in Saturn's ionosphere caused by explosive surges of water from Enceladus?, *Geophys. Res. Lett.*, *34*, L12202, doi:10.1029/2007GL029381.

Moore, L. E., M. Mendillo, I. C. F. Mueller-Wodarg, and D. L. Murr (2004), Modeling of global variations and ring shadowing in Saturn's ionosphere, *Icarus*, *172*, 503–520.

Moore, L., A. F. Nagy, A. J. Kliore, I. Müller-Wodarg, J. D. Richardson, and M. Mendillo (2006), Cassini radio occultations of Saturn's ionosphere: Model comparisons using a constant water flux, *Geophys. Res. Lett.*, *33*, L22202, doi:10.1029/2006GL027375.

Moore, L., M. Galand, I. Mueller-Wodarg, R. V. Yelle, and M. Mendillo (2008), Plasma temperatures in Saturn's ionosphere, *J. Geophys. Res.*, *113*, A10306, doi:10.1029/2008JA013373.

Moore, L., M. Galand, I. Mueller-Wodarg, and M. Mendillo (2009), Response of Saturn's ionosphere to solar radiation: Testing parameterizations for thermal electron heating and secondary ionization processes, *Planet. Space Sci.*, *57*(14–15), 1699–1705, doi:10.1016/j.pss.2009.05.001.

Moses, J. I., and S. F. Bass (2000), The effects of external material on the chemistry and structure of Saturn's ionosphere, *J. Geophys. Res.*, *105*, 7013–7052.

Moses, J. I., E. Lellouch, B. Bézard, G. R. Gladstone, H. Feuchtgruber, and M. Allen (2000), Photochemistry of Saturn's atmosphere, II. Effects of an influx of external oxygen, *Icarus*, *145*, 166–2002.

Mueller-Wodarg, I. C. F., M. Mendillo, R. V. Yelle, and A. D. Aylward (2006), A global circulation model of Saturn's thermosphere, *Icarus*, *180*, 147–160.

Nagy, A. F., et al. (2006), First results from the ionospheric radio occultations of Saturn by the Cassini spacecraft, *J. Geophys. Res.*, *111*, A06310, doi:10.1029/2005JA011519.

Nagy, A. F., A. J. Kliore, M. Mendillo, S. Miller, L. Moore, J. I. Moses, I. Mueller-Wodarg, and D. Shemansky (2009), Upper atmosphere and ionosphere of Saturn, in *Saturn From Cassini-Huygens*, edited by M. K. Dougherty, L. W. Esposito, and S. M. Krimigis, pp. 181–202, Springer, New York.

Nichols, J. D., J. T. Clarke, S. W. H. Cowley, J. Duval, A. J. Farmer, J.-C. Gérard, D. Grodent, and S. Wannawishian (2008), Oscillation of Saturn's southern auroral oval, *J. Geophys. Res.*, *113*, A11205, doi:10.1029/2008JA013444.

Nichols, J. D., et al. (2009), Saturn's equinoctial auroras, *Geophys. Res. Lett.*, *36*, L24102, doi:10.1029/2009GL041491.

Pontius, D. H., and T. W. Hill (2006), Enceladus: A significant plasma source for Saturn's magnetosphere, *J. Geophys. Res.*, *111*, A09214, doi:10.1029/2006JA011674.

Prangé, R., T. Fouchet, R. Courtin, J. E. P. Connerney, and J. C. McConnell (2006), Latitudinal variation of Saturn photochemistry deduced from spatially-resolved ultraviolet spectra, *Icarus*, *180*, 379–392.

Russell, C. T., and M. K. Dougherty (2010), Magnetic fields of the outer planets, *Space Sci. Rev.*, *152*, 251–269, doi:10.1007/s11214-00909621-7.

Schunk, R. W., and A. F. Nagy (2009), *Ionospheres: Physics, Plasma Physics, and Chemistry*, 2nd ed., 628 pp., Cambridge Univ. Press, Cambridge, U. K.

Smith, G. R., D. E. Shemansky, J. B. Holberg, A. L. Broadfoot, B. R. Sandel, and J. C. McConnell (1983), Saturn's upper atmosphere from the Voyager 2 EUV solar and stellar occultations, *J. Geophys. Res.*, *88*, 8667–8678.

Stallard, T., S. Miller, H. Melin, M. Lystrup, S. W. H. Cowley, E. J. Bunce, N. Achilleos, and M. Dougherty (2008), Jovian-like aurorae on Saturn, *Nature*, *453*, 1083–1085, doi:10.1038/nature07077.

Tyler, G. L., V. R. Eshleman, J. D. Anderson, G. S. Levy, G. F. Lindal, G. E. Wood, and T. A. Croft (1981), Radio science investigation of the Saturn system with Voyager 1: Preliminary results, *Science*, *212*, 201–206.

Tyler, G. L., V. R. Eshleman, J. D. Anderson, G. S. Levy, G. F. Lindal, G. E. Wood, and T. A. Croft (1982), Radio science with Voyager 2 at Saturn—Atmosphere and ionosphere and the masses of Mimas, Tethys, and Iapetus, *Science*, *215*, 553–558.

Waite, J. H., S. K. Atreya, and A. F. Nagy (1979), The ionosphere of Saturn—Predictions for Pioneer 11, *Geophys. Res. Lett.*, *6*, 723–726.

Woods, T. N. (2008), Recent advances in observations and modeling of the solar ultraviolet and X-ray spectral irradiance, *Adv. Space Res.*, *42*, 895–902, doi:10.1016/j.asr.2007.09.026.

Woods, T. N., et al. (2000), TIMED Solar EUV Experiment, *Phys. Chem. Earth Part C*, *25*, 393–396.

Woods, T. N., F. G. Eparvier, S. M. Bailey, P. C. Chamberlin, J. Lean, G. J. Rottman, S. C. Solomon, W. K. Tobiska, and D. L. Woodraska (2005), The Solar EUV Experiment (SEE): Mission overview and first results, *J. Geophys. Res.*, *110*, A01312, doi:10.1029/2004JA010765.

M. Galand and I. Mueller-Wodarg, Department of Physics, Imperial College London, London SW7 2AZ, UK.

A. Kliore, Radio Science Systems, Jet Propulsion Laboratory, MS 161-260, 4800 Oak Grove Dr., Pasadena, CA 91109, USA.

M. Mendillo and L. Moore, Center for Space Physics, Boston University, Boston, MA 02215, USA. (moore@bu.edu)